JGR Oceans

RESEARCH ARTICLE
10.1029/2021JC018075

Special Section:
The Arctic: An AGU Joint Special Collection

Air-Sea Interactions and Water Mass Transformation During a Katabatic Storm in the Irminger Sea

O. Gutjahr[1,2], J. H. Jungclaus[2], N. Brüggemann[1,2], H. Haak[2], and J. Marotzke[2,3]

[1]Institut für Meereskunde, Universität Hamburg, Hamburg, Germany, [2]The Ocean in the Earth System, Max Planck Institute for Meteorology, Hamburg, Germany, [3]Center for Earth System Research and Sustainability (CEN), Universität Hamburg, Hamburg, Germany

Key Points:

- For the first time, the direct effect of a katabatic storm on the Irminger Sea has been simulated in a global climate model
- The katabatic storm induces strong heat loss and dense water formation over the Irminger shelf (Sermilik Trough) and in the boundary current
- Dense water forming in the western boundary current during katabatic storms contributes to the lightest upper North Atlantic Deep Water

Correspondence to:
O. Gutjahr,
oliver.gutjahr@mpimet.mpg.de

Citation:
Gutjahr, O., Jungclaus, J. H., Brüggemann, N., Haak, H., & Marotzke, J. (2022). Air-sea interactions and water mass transformation during a katabatic storm in the Irminger Sea. *Journal of Geophysical Research: Oceans*, *127*, e2021JC018075. https://doi.org/10.1029/2021JC018075

Received 19 OCT 2021
Accepted 17 APR 2022

Abstract We use a global 5-km resolution model to analyze the air-sea interactions during a katabatic storm in the Irminger Sea originating from the Ammassalik valleys. Katabatic storms have not yet been resolved in global climate models, raising the question of whether and how they modify water masses in the Irminger Sea. Our results show that dense water forms along the boundary current and on the shelf during the katabatic storm due to the heat loss caused by the high wind speeds and the strong temperature contrast. The dense water contributes to the lightest upper North Atlantic Deep Water as upper Irminger Sea Intermediate Water and thus to the lower limb of the Atlantic Meridional Overturning Circulation (AMOC). The katabatic storm triggers a polar low, which in turn amplifies the near-surface wind speed due to the superimposed pressure gradient, in addition to acceleration from a breaking mountain wave. Overall, katabatic storms account for up to 25% of the total heat loss (20 January 2020 to 30 September 2021) over the Irminger shelf of the Ammassalik area. Resolving katabatic storms in global models is therefore important for the formation of dense water in the western boundary current of the Irminger Sea, which is relevant to the AMOC, and for the large-scale atmospheric circulation by triggering polar lows.

Plain Language Summary Katabatic storms are outbursts of cold air associated with strong winds from coastal valleys of Greenland, in particular from the Ammassalik valleys in southeast Greenland. These storms are not resolved in global climate models because of their small spatial extent. However, they are important for the formation of dense water on the Irminger Sea shelf, because they induce a substantial heat loss from the coastal water. In this study, we resolve katabatic storms for the first time in a global climate model and analyze the water transformation caused by a single storm before quantifying the importance of katabatic storms for the entire simulation period. We find that a water mass is formed during the katabatic storm that is dense enough to contribute to the cooling and sinking of the global conveyor belt in the subpolar North Atlantic. Overall, katabatic storms account for up to 25% of the heat loss over the Irminger shelf of the Ammassalik area.

1. Introduction

Recent observations made with the Overturning in the Subpolar North Atlantic Program (OSNAP) array (Lozier et al., 2017) allowed for the first time to directly relate deep water mass formation in the subpolar North Atlantic and overturning variability. These data indicate that water mass transformation east of Greenland is largely responsible for the overturning of the Atlantic Meridional Overturning Circulation (AMOC) and its variability (Li et al., 2021; Lozier et al., 2019). However, the exact role of the Irminger and Labrador Sea in AMOC variability is still controversial. In particular, it is discussed whether deep water formation in the Labrador Sea contributes only marginally to AMOC variability (Desbruyères et al., 2019; Li et al., 2021; Menary et al., 2020), whether there has been a shift in deep water formation from the Labrador to the Irminger Sea over the past decade (Rühs et al., 2021), or whether deep water formation in the Labrador Sea dominates multidecadal AMOC variability, while formation in the Irminger Sea influences high-frequency variability (Yeager et al., 2021).

In the Irminger Sea, strong surface heat and momentum fluxes were found to be most important for generating density anomalies in the boundary currents, such as the East Greenland-Irminger Current (EGIC) or over the Reykjanes Ridge (LeBras et al., 2020; Petit et al., 2020). Based on OSNAP, a light mode convective water named upper Irminger Sea Intermediate Water (uISIW; $\sigma_\theta = 27.65$–27.73 kg m^{-3}) has been identified forming at the edge of the EGIC (LeBras et al., 2020). This intermediate water contributes to light upper North Atlantic Deep Water

(uNADW), defined as $\sigma_\theta = 27.55–27.73$ kg m^{-3} (Li et al., 2021) along with the denser water masses formed by deep convection in the basin interior (Bacon et al., 2003; de Jong et al., 2012, 2018; Pickart et al., 2003) and overflows from the Nordic Seas (Chafik & Rossby, 2019). These dense water anomalies in the boundary current are transported southward into the Labrador Sea, where they correlate strongly with AMOC variability (Desbruyères et al., 2019; Menary et al., 2020; Petit et al., 2020).

However, the surface fluxes producing these density anomalies are likely underestimated in current global climate models, such as those involved in CMIP6 (Eyring et al., 2016) or in CMIP6 HighResMIP (Haarsma et al., 2016). These strong surface fluxes are caused by mesoscale wind systems with horizontal length scales of about 200 km (e.g., Moore & Renfrew, 2005), and are therefore not or insufficiently resolved (Moore et al., 2015). The Irminger Sea is known as an area where strong near-surface winds occur (Sampe & Xie, 2007). Three mesoscale wind systems are to be mentioned in connection with the steep topography of Greenland. First, Greenland tip jets (Doyle & Shapiro, 1999; Moore & Renfrew, 2005; Pickart et al., 2003) at Cape Farewell occur when a synoptic low is located east of Cape Farewell and the flow is forced around it, causing it to accelerate. Because of its high wind speeds, westerly tip jets were found to be important for preconditioning and triggering open-ocean deep convection in the Irminger Gyre (Våge et al., 2011) of the southwestern Irminger Sea (Bacon et al., 2003; Pickart et al., 2003; Våge et al., 2009). Hourly net heat fluxes during tip jet events can thereby exceed 800 W m^{-2} (Josey et al., 2019). Second, barrier winds form south of Denmark Strait when the air mass impinges onto the steep coast of Greenland, creating a geostrophic pressure gradient that accelerates the flow along the coast to the southwest (Moore & Renfrew, 2005). And third, katabatic winds from the Greenland ice sheet. Both barrier winds and katabatic winds can cause marine cold air outbreaks (MCAO, Kolstad et al., 2009), either by advecting cold polar air mass from the sea ice or from Greenland's ice sheet over the Irminger Sea.

Katabatic winds are density-driven currents originating from large ice sheets, such as in Greenland, due to radiative cooling of the surface boundary layer. They dominate the near-surface wind field and their velocity is highest near the ice sheet margins. The strongest downslope katabatic winds occur frequently in the Ammassalik area on the southeast coast of Greenland, where the katabatic flow converges in the narrow fjords and accelerates because of the steep topography (Heinemann & Klein, 2002). This gravitational acceleration becomes stronger the colder and thus denser the air is. When a synoptic cyclone is located over the Irminger Sea, the overlying geostrophic flow can strengthen the pure katabatic flow to gale force, sometimes even hurricane force, which then causes severe destruction (Oltmanns et al., 2014; Rasmussen, 1989). Often these two mechanisms work together to form a katabatic storm. However, a third mechanism is the breaking of mountain or lee waves over the steep slopes of southeast Greenland (Oltmanns et al., 2015), which transfer momentum into the boundary layer and further accelerate the katabatic flow. These hazardous katabatic storms or “piteraqs” (Greenlandic) are a regular phenomenon. The most severe storm on record hit the community of Tasiilaq (Ammassalik) in February 1970 with a peak velocity of nearly 90 m s^{-1}.

Over the Irminger Sea, katabatic winds and storms from the Ammassalik valleys cause a strong loss of heat and buoyancy of the shelf water and EGIC due to the high wind speeds and the cold and dry air they carry over the relatively warm ocean. They contribute to about one fifth of the total winter heat loss (Oltmanns et al., 2014). Resolving katabatic storms could therefore affect the dense water formation in the Irminger Sea and hence its role for AMOC variability.

Katabatic winds can trigger mesocyclones over the Irminger Sea (Klein & Heinemann, 2002), also called polar lows (Kolstad, 2011; Moreno-Ibáñez et al., 2021). Polar lows frequently form over the Irminger Sea (Bracegirdle & Gray, 2008; Kolstad, 2011; Stoll et al., 2018; Zahn & von Storch, 2008), which is related to cyclogenesis in the lee of Greenland's high orography (Blechschmidt et al., 2009; Kristjánsson et al., 2011). In particular, two mechanisms are at work (Klein & Heinemann, 2002). First, convergence of the katabatic flow in the valleys lead to vortex stretching that enhances cyclonic vorticity, which is then transported eastward by the horizontal flow. Second, advection of cold air from the Greenland ice sheet over the relatively warm Irminger Sea leads to high sensible and latent heat fluxes, whose divergences reduce the atmospheric stratification. If clouds form over the Irminger Sea because of the large latent heat fluxes, atmospheric stratification is further reduced due to release of latent heat. Katabatic winds from Ammassalik therefore increase low-level baroclinicity that favors the formation of polar lows. On average, about 5–11 polar lows form in the Irminger Sea per winter, depending on the detection method and data set analyzed (Zahn & von Storch, 2008; Kolstad, 2011), while katabatic storms in the Ammassalik area occur about seven times per year, reaching about 20 m s^{-1} (Oltmanns et al., 2014).

If sea ice is present, katabatic winds from the Ammassalik valleys can open coastal polynyas (Heinemann, 2003). The brine released during the formation of new sea ice then contributes to even denser shelf waters. Katabatic winds may also be important for fluxing fresh shelf water of Arctic origin into the interior basin of the Irminger Sea, thereby affecting the stratification. How exactly freshwater is transported off-shelf is still unclear, but wind is thought to be the main driver (Duyck & de Jong, 2021).

Resolving katabatic storms and small-scale orographic features in global climate models is therefore crucial for the cooling and densification of the EGIC, but also for the feedback of small-scale processes to the synoptic scale in terms of polar low formation and exchange of momentum and energy. Because of the teleconnectivity that the Irminger Sea exerts on the AMOC and the large-scale atmospheric circulation, a global coupled model is needed to capture these interactions. However, the atmospheric resolution of CMIP6 models is on the order of 50–200 km, with some exceptions of 25 km for individual HighResMIP models. Katabatic winds and other mesoscale wind systems around Greenland, such as tip jets, require model resolutions of less than 10–15 km to be adequately represented (DuVivier & Cassano, 2013; Gutjahr & Heinemann, 2018; Oltmanns et al., 2015). A resolution of 5 km is even better to capture the channeling effects in the narrow fjords and the momentum transfer by breaking mountain waves over the steep coastal slopes (Oltmanns et al., 2015). Katabatic winds further require a high vertical resolution in the surface boundary layer where also low-level jets form (Heinemann, 2003). In addition, a nonhydrostatic dynamical core is needed to simulate the strong vertical velocities during a katabatic storm, especially where mountain waves break causing a katabatic jump and generating gravity waves.

High resolution is required to resolve katabatic storms around Greenland, which is why they have so far only been studied with regional atmosphere models (e.g., Klein & Heinemann, 2002; Oltmanns et al., 2014, 2015). Even though high resolution can be achieved in regional models, they have two severe limitations. First, they were used as stand-alone, that is, they were not coupled to an ocean model, thereby neglecting air-sea interactions with the ocean, including changes to the circulation and the water mass characteristics. Second, because of their limited domain they do not allow for feeding back the effects of the small scales to the large scales, thereby neglecting teleconnections. Although the interactions across scales are sometimes realized in regional models by so-called two-way nesting, the problem remains that the rest of the globe is not affected by the resolved small scales within the domain. Similar arguments apply to studies with ocean stand-alone simulations, which must be driven by atmospheric data that cannot respond to feedbacks with the ocean and are often too coarse to represent the mesoscale winds around Greenland (e.g., Paquin et al., 2016).

Because the resolution of global climate models has been too coarse to resolve katabatic storms (Mc Innes et al., 2011), their influence on EGIC has likely been underestimated. Although there were attempts to account for their effects on the ocean circulation (Condron et al., 2008), such parameterizations were never widely used in global models. Here we analyze for the first time a katabatic storm or piteraq that triggers a polar low, interacts with it and causes water mass transformation in the Sermilik Trough (ST) and EGIC. We exploit a frontier simulation with the global storm-resolving and eddy-resolving (5 km) ICON-ESM, which is almost 2 years long. A more detailed overview of the simulation will be presented elsewhere. The analyzed katabatic storm is the most intense in the simulation, which is why we chose it for our case study. Even though the simulation is too short to link density anomalies in the boundary current to the AMOC, the model is potentially able to simulate this linkage.

The remainder of the manuscript is organized as follows: in Section 2 we describe the model configuration. Section 3 outlines the development of the katabatic storm. Section 4 describes the air-sea interactions during the storm and induced water transformations. In Section 5, we widen the picture to all katabatic storms in the simulation and quantify their effect on the net heat loss, before we conclude in Section 6.

2. Model Configuration

We analyze the development of a katabatic storm in the Irminger Sea and its induced air-sea fluxes and water mass transformation in a frontier simulation made with ICON-ESM (ICOsahedral Nonhydrostatic—Earth System Model; Giorgetta et al., 2018; Jungclaus et al., 2022; Korn, 2017; Zängl et al., 2015), which is participating in the second phase of the DYnamics of the Atmospheric general circulation On Nonhydrostatic Domains (DYAMOND) Winter initiative (Stevens et al., 2019, and https://www.esiwace.eu/services/dyamond/winter). The model is globally coupled and was run at a horizontal resolution of 5 km, both in the nonhydrostatic atmospheric

component (ICON-A) and in the hydrostatic ocean/sea ice component (ICON-O). The grid resolution is thereby defined as the square root of the cell area of the spherical triangles (Zängl et al., 2015). Both components use a high vertical resolution. ICON-A is run with 90 terrain-following, hybrid sigma levels, with the top layer at 75 km height, which corresponds to the operational weather forecast configuration at Deutscher Wetterdienst (DWD). Thirteen levels are distributed within the lower 2,000 m over the Irminger Sea and 20 levels over land in the Ammassalik area. ICON-O uses 128 z-levels without a partial bottom cell parameterization. Ninety-six levels are distributed within the upper 500 m.

A main purpose of the DYAMOND (Winter) initiative is to run atmosphere models at a convection and storm-resolving resolution ($\leq$5 km) and the ocean models at a similar resolution. The vertical resolution must be at least 75 levels in both spheres in order to study the mesoscale ocean-atmosphere coupling. Although the model resolution approaches the km scale, the smallest scale that is fully resolved in the model—the effective resolution—is much larger than the grid spacing or nominal model resolution. The effective resolution is usually determined by comparing modeled and observed kinetic energy spectra (Skamarock, 2004). For ICON-A, the effective resolution is about 7 times the mesh size (Neumann et al., 2019; Zängl et al., 2015), which corresponds to 35 km for our configuration. Below this scale, kinetic energy is dissipated due to physical parameterizations, orographic smoothing, numerical diffusion, and aliasing effects (Klaver et al., 2020; Neumann et al., 2019). Therefore, small-scale atmospheric processes, such as convection, orographic drag, or nonhydrostatic waves (Reinecke & Durran, 2009), are still partially unresolved in this model configuration. However, studies with regional models have shown that a nominal model resolution of less than 10–15 km is sufficient to resolve the main features of mesoscale wind systems around Greenland (DuVivier & Cassano, 2013; Gutjahr & Heinemann, 2018) and that 5 km is sufficient for the representation of katabatic storms (Oltmanns et al., 2014, 2015).

For ICON-O there has been no quantification of the effective resolution yet. With reference to the first baroclinic Rossby deformation radius calculated by LaCasce and Groeskamp (2020), which also takes bathymetry into account, we find a required resolution to resolve eddies of about 1/25° to 1/12° in the Irminger Sea (about 5–2 km at 60°N) and 1/50° (about 1 km) over the shelf.

ICON-A was run with the ECHAM6.3 physics (Giorgetta et al., 2018) and not with the Numerical Weather Prediction (NWP) physics used at DWD. The reason is that the ECHAM6.3 physics is largely energy conserving, which is a necessity for studying coupled processes and climate. However, to account for the storm-resolving resolution, several adjustments were made to the physical parameterizations in ICON-A. First, the atmospheric deep convection scheme was switched off. Further, parameterizations of subgrid-scale orographic effects (blocking and gravity wave drag) and nonorographic gravity wave drag were switched off and cloud microphysics were calculated using a three-category ice scheme, referred to as the graupel scheme. On the other hand, atmospheric subgrid-scale turbulence was parameterized with the 3D-Smagorinsky scheme, which has been implemented into ICON-A for large eddy simulation applications (Dipankar et al., 2015). In ICON-O, the mesoscale eddy parameterization (Gent-McWilliams (GM) closure) was switched off and vertical mixing was parameterized with the turbulent kinetic energy (TKE) closure (Blanke & Delecluse, 1993; Gaspar et al., 1990).

Before coupling, both components were spun up separately. The atmosphere was initialized from the global (9 km) European Centre for Medium Range Weather Forecasts (ECMWF) Integrated Forecasting System (IFS) analysis corresponding to 20 January 2020. Spinning up the ocean is more expensive. Therefore, the following strategy was used for this first 5 km coupled simulation. The initial fields were taken from PHC3.0 (Steele et al., 2001) and interpolated to a coarser 10 km grid. The ocean was spun up on this coarser grid using a combination of different atmospheric forcing data. First, 25 cycles were run with OMIP forcing, a climatology based on the ERA-40 years 1958–2001 (Simmons & Gibson, 2000), followed by NCEP (Kalnay et al., 1996) from 1948 to 2000 and ERA5 (Hersbach et al., 2020) from 2000 to 2010. Then, the ocean state was interpolated from the 10 km to the 5 km grid and the 10 recent years (2011–2020) were forced with ERA5 to ensure the development of background features, such as ocean mesoscale eddies or currents. We note that the spin-up was produced with an older model version and was not repeated with the version of the production run due to computational costs.

Once coupled, atmospheric fluxes were exchanged every 15 min. The model was run for 21 simulation months, starting from 20 January 2020 and ending on 30 September 2021. However, we focus on the first winter and in particular on the 29 February when the katabatic storm develops. Before analyzing the fields, all output data have been interpolated by the nearest neighbor method onto a regular grid of 0.05°.

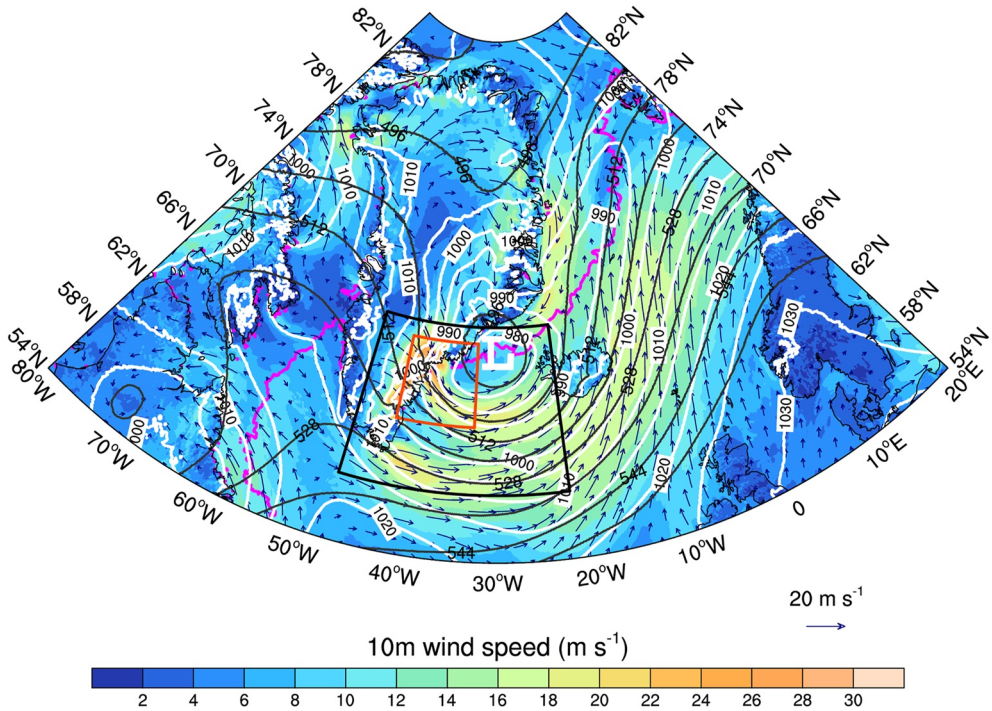

Figure 1. Synoptic situation on simulation day for 29 February 2020 in ICOsahedral Nonhydrostatic—Earth System Model (ICON-ESM). Shown is the daily mean of 10 m wind speed (color shaded) and the wind vectors. Overlain is the daily mean-sea level pressure in hPa (white contours), the geopotential height at 500 hPa in gpdm (dark gray contours), and the 15% sea ice concentration (magenta contour). The reference scale of the wind vectors is given at the bottom right. The "L" symbol marks the center of the polar low that is moving toward Denmark Strait. The black box marks the area of the Irminger Sea and the orange box the Ammassalik area.

Using a global simulation has the advantage of avoiding arbitrary domain boundaries, such as in regional models, which would inevitably introduce artifacts that could influence the process under investigation (Giorgi, 2019; Leduc & Laprise, 2009). In addition, due to the global high resolution, the synoptic fields and the background state of the ocean are expected to be more realistic than in comparable downscaling studies, where only the nested simulation is run at high resolution, while the parent simulation has a much coarser resolution. In addition, by resolving the mesoscale, feedbacks to the large scales are captured, thereby changing the synoptics. This feedback is thereby not restricted to the domain of interest but acts globally, with effects on remote areas.

3. Synoptic Overview and Katabatic Storm Development

We analyze a katabatic storm appearing on the simulation day of 29 February 2020 and that has no real-time counterpart. This storm is the strongest of five similar events within the two simulation years (see Section 5), and its effect on the Irminger Sea is most pronounced, which is why it was chosen for our case study. During the simulation, no open-ocean deep convection occurs in the Irminger Sea (see Section 4.3), and deeper mixed layers during winter are only simulated along the western flank of the Reykjanes Ridge (600–900 m) and along the EGIC (500–1,300 m).

The storm develops when an upper-level trough crosses southeast Greenland. Within the westerly flow, a lee trough (LT) forms east of Cape Farewell, Greenland's southernmost tip. Within the LT, the katabatic flow from the Ammassalik area triggers a polar low. The synoptic pressure gradient on the backside of the polar low amplifies the katabatic winds until the storm reaches near-surface wind speeds of more than 26 m s^{-1} (Figure 1) and almost 50 m s^{-1} in the low-level jet at the boundary layer top. The polar low produces a strong near-surface pressure gradient, resulting in a westerly tip jet at Cape Farewell on 28 February at 18 UTC to 29 February at 0 UTC. As the polar low moves northeastward toward Denmark Strait on 29 February at 18 UTC, the pressure gradient at Cape Farewell decreases and so does the tip jet, while the katabatic flow becomes strongest and barrier winds

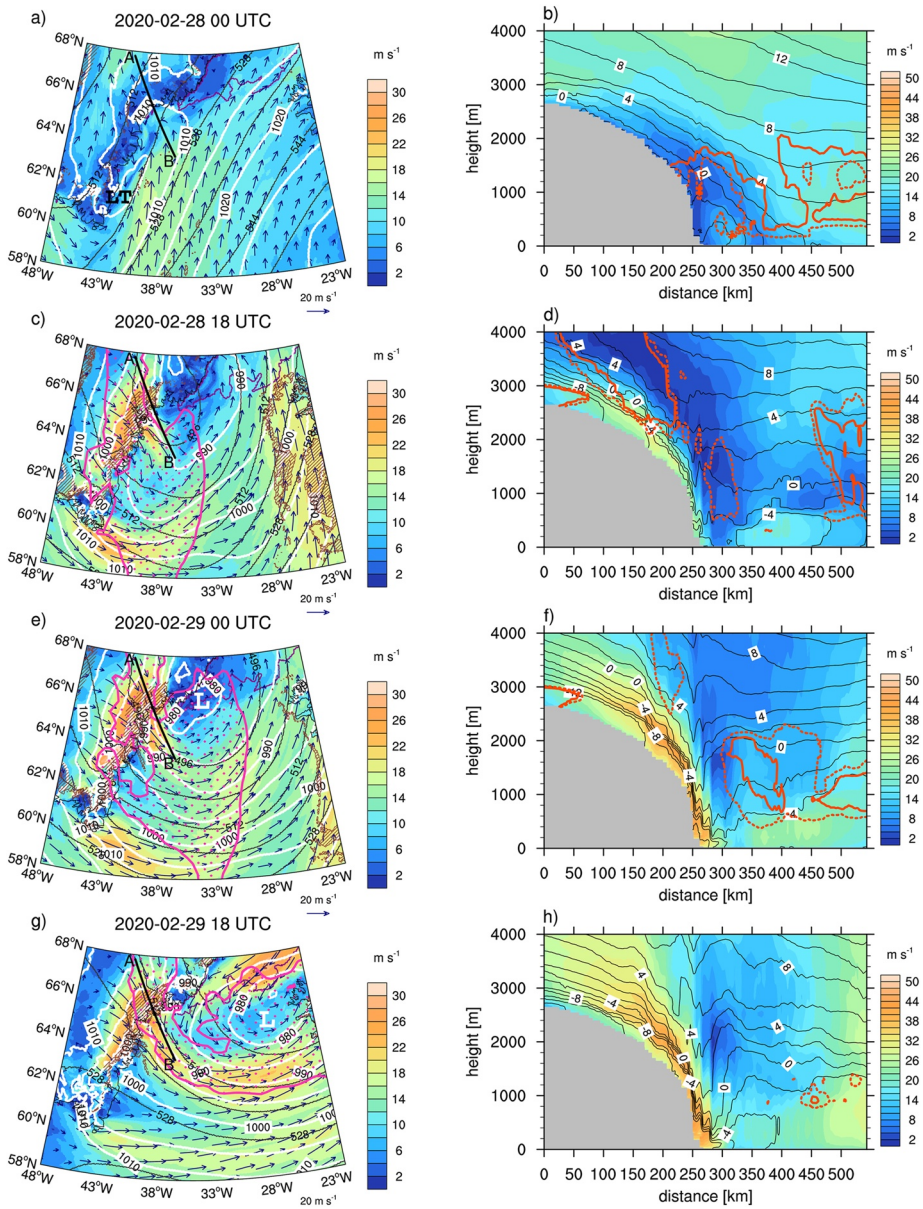

Figure 2. Development of the katabatic storm on 28 and 29 February 2020 in the Irminger Sea as simulated by ICON-ESM. The first column (a, c, e, and g) shows the 10 m wind speed (6-hourly mean; color shaded) and vectors, overlain by the mean-sea level pressure in hPa (white contours, every 5 hPa), the potential vorticity at 500 hPa (≥2 PVU; 1 PVU = 10^{-6} K m^2 kg^{-1} s^{-1}; magenta and stippling), and the sea ice edge (15% ice concentration, purple contour). "LT" in (a) marks the lee trough east of Cape Farewell, and "L" in (e, g) the position of the polar low. Brown hatching marks areas where the Eady growth rate averaged over the lowest 2,000 m is larger than $0.5 \cdot 10^{-4}$ s^{-1}. The second column (b, d, f, and h) shows the transects of wind speed (shaded color), potential temperature in $°C$ (black contours) and cloud cover (25% as dashed and 50% as solid orange contours) along the Ikertivaq valley in the Ammassalik area (black line in first column).

form in Denmark Strait. This succession of events is quite common in the Irminger Sea and reflects the passage of a low.

On 28 February 2020 at 00 UTC, the center of the upper-level trough is located over western Greenland (Figure 2a). The southeast coast of Greenland is below the cyclonic side of the diffluence zone of the jetstreak and hence an area favorable for upward motion and cyclogenesis. Upper-level divergence and differential vorticity advection cause upward motion diagnosed via the vorticity term in the ω-equation. A lee trough forms east of Cape Farewell (Figure 2a) and further preconditions the southeast coast of Greenland for cyclogenesis (Kristjánsson

et al., 2011). These lee troughs form frequently east of Cape Farewell in response to vortex stretching and potential vorticity (PV) conservation (Mc Innes et al., 2009) when the westerly flow descends adiabatically from the high orography of Greenland (Kristjánsson et al., 2011). A vertical transect along the Ikertivaq valley (Figure 2b) shows only weak winds near the surface and a stable stratification with cloud cover below 2,000 m.

Within the next 18 hr, the upper-level trough crosses southern Greenland and its center deepens to 496 gpdm over the Irminger Sea (Figure 2c), showing a strong cyclonic PV anomaly with more than 2 PVU at 500 hPa. At the surface, the pressure is falling in response to the upper-level divergence that induces low-level convergence (Bracegirdle & Gray, 2009; Hoskins et al., 1985). Katabatic flow is initiated by a superimposed pressure gradient over the Ammassalik valleys and cold air is drained from the Greenland ice sheet (Figure 2d). Near the coast, the katabatic flow channels in the narrow valleys and accelerates. This converging flow constitutes a low-level baroclinic instability and enhances cyclonic vorticity due to vortex stretching, thereby increasing the PV anomaly (Klein & Heinemann, 2002). As a measure for baroclinicity we calculate the maximum Eady growth rate ($\sigma_{\max}$ in s^{-1}; Dierer & Schluenzen, 2005; Eady, 1949; Lindzen & Farrell, 1980) that describes how well deep pressure systems can develop in a weather situation over a specific area, with positive values favoring cyclogenesis:

$$\sigma_{\max} = 0.398 f \partial_z \boldsymbol{V}_h N^{-1}, \tag{1}$$

with f the Coriolis parameter, $\partial_z \boldsymbol{V}_h$ the vertical wind shear, and $N = \sqrt{g/\theta \partial_z \theta}$ the buoyancy frequency that depends on the gravitational constant g and the vertical gradient of the potential temperature θ. The Ammassalik area is clearly a region of low-level baroclinicity as indicated by the positive Eady growth rate in Figure 2c.

Within the next 6 hr, the katabatic flow from Ammassalik triggers a polar low with closed isobars on 29 February at 00 UTC and a core pressure of less than 980 hPa (Figure 2e). Converging flow, differential cold air advection decreasing with height in the Ammassalik area trigger the formation of the polar low (Klein & Heinemann, 2002) near the sea ice edge, where polar lows frequently form and intensify (Bracegirdle & Gray, 2009; Dierer & Schluenzen, 2005). There is also a two-way interaction of the polar low-level and the upper-level trough. The strong low-level cold air advection from the Ammassalik valleys west of the polar low and advection of warmer air to its east induces a cyclonic rotation that interacts with the upper-level trough, which intensifies and leads to additional pressure fall near the surface (Van Delden et al., 2003). This additional pressure fall also explains the frequently observed rapid development of polar lows.

The Irminger Sea is known for polar low genesis and exhibits strong vertical temperature differences (Kristjánsson et al., 2011). Although there is no universal definition for a polar low (Kolstad, 2011), Blechschmidt et al. (2009) defined two criteria: (a) temperature difference between the sea surface and at 500 hPa (SST $- T_{500}$) of more than 48 K and (b) an upper-level cyclonic PV anomaly. From 6-hourly averages, we find both criteria roughly fulfilled with SST $- T_{500} = 45$ K (not shown) and a positive PV anomaly of more than 2 PVU at 500 hPa. Note that there are other thresholds used, such as 43 K (Xia et al., 2012) or 40 K (Landgren et al., 2019), or other definitions, such as the MCAO index (SST $- T_{700}$; Kolstad et al., 2009). For our study, the exact threshold or definition is not decisive.

On the back side of the polar low, the superimposed pressure gradient intensifies, further accelerating the katabatic flow (Figure 2e) and draining increasingly cold air from the Greenland ice sheet. The cold air spreads as a tongue over the Irminger Sea, where it warms and causes atmospheric convection with cloud formation (Figure 2f). In addition, a mountain or lee wave breaks at the steep slope of the topography (roughly at 250 km distance) and transfers momentum downwards into the boundary layer (Oltmanns et al., 2015) that further accelerates the katabatic flow. Once the polar low reaches mature state (Figures 2g and 2h), the wind speed peaks with hurricane intensity of almost 50 m s^{-1} within the low-level jet near the top of the boundary layer. Although the highest near-surface wind speeds occur over the shelf, the storm affects the entire Irminger Sea, even reaching Iceland (Figure 2g).

These results suggest that four processes interact in the formation of the polar low and cause this katabatic storm: (a) favorable conditions for cyclogenesis due to an upper-level trough crossing South Greenland (upper-level divergence and positive vorticity advection or PV anomaly), (b) a LT east of Cape Farewell generating cyclonic vorticity due to vortex stretching, (c) triggering of a polar low due to converging flow from the Ammassalik valleys and superimposed pressure gradient force of the polar low that amplifies the katabatic flow, and (d) a breaking mountain wave that transfers momentum downward into the surface boundary layer and causes

additional acceleration. Although we cannot generalize from this case study, it seems that all these processes are of importance in the polar low formation in the Irminger Sea and for generating katabatic storms of hurricane intensity.

4. Air-Sea Interactions and Water Mass Transformation Over the Shelf and in the Irminger Sea

4.1. Air-Sea Interactions

The katabatic storm with its high wind speeds is expected to substantially modify the water of the southeast Greenland shelf, but also the western boundary current, that is, EGIC, and the upper ocean of the Irminger Basin, because the tongue of cold air and high wind speeds extends across the entire basin and even reaches the western flank of the Reykjanes Ridge (Figure 2g).

The katabatic storm (daily means on 29 February 2020; Figure 3a) consists of two cones of high wind speeds that merge over the southeast Greenland shelf, one from Ikertivaq valley and the other from the Køge Bugt Fjord. We focus on the flow from the Ikertivaq valley because it directly passes over the Sermilik Trough (ST), a bathymetric feature that reaches depths of about 800 m (An et al., 2019). The ST has recently received attention because drifter data revealed that the East Greenland Current (EGC) steers northwards on its northern flank, where it interacts with the East Greenland Coastal Current (EGCC, Duyck & de Jong, 2021). Indeed, we find similar pathways of the EGC or EGIC in our simulation (Figure 3b) that agree well with trajectories of these drifters. The main part of the EGIC flows along the shelf break, but a smaller fraction steers northward into the ST with even a pathway that directly crosses the trough, as described by Duyck and de Jong (2021).

The inflow of the relatively warm EGIC along the northern flank of the ST results in warmer sea surface temperatures (SST) of about 3–4.5 °C (Figure 3c). These warmer SSTs in the northern ST could be the reason why there is no sea ice present in the Ammassalik area. After mixing with the colder and fresher EGCC, but also because of substantial heat loss to the atmosphere (Figures 3e–3f), the SSTs are colder (1.5–3 °C) in the return flow in the southern ST. The sensible and latent heat fluxes reach daily mean values of 1,000 W m^{-2} over the ST during the event because of strong wind speeds and large temperature and moisture contrasts. The high wind speeds exert strong wind stress on the upper ocean (Figure 3).

At the shelf break, the cold katabatic flow encounters the warmer waters of the recirculating Irminger Current and the turbulent heat fluxes peak for a second time with values of about 700 W m^{-2} for the sensible heat flux and 600 W m^{-2} for the latent heat flux. The sensible heat flux is higher during the event because the air-sea contrast is stronger for temperature than for moisture.

These values are somewhat larger than what was found for turbulent heat fluxes during typical westerly tip jets at Cape Farewell. For instance, Våge et al. (2009) found turbulent heat fluxes of about 400 W m^{-2} and Moore (2014) reports values of up to 600 W m^{-2}, and most recently, Josey et al. (2019) finds daily values of net heat loss of about 400–600 W m^{-2} from mooring data in the Irminger Sea. However, for katabatic storms, Oltmanns et al. (2015) found about 1,000 W m^{-2} for the total heat flux during a katabatic storm event based on simulations with a regional atmosphere model. The higher turbulent heat fluxes during katabatic storms could be explained by higher temperature and moisture contrasts than during tip jet events. The cold and dry air draining from the Greenland ice sheet does encounter warmer ocean surface temperature for the first time over the Irminger shelf, whereas the cold air during tip jet events mainly results from cold air outbreaks from sea ice over the Labrador Sea and could therefore warm and moisten on its way over the ocean to Cape Farewell, reducing the vertical temperature and humidity gradients.

4.2. Vertical Transects Along the Ikertivaq Valley and Sermilik Trough

Transects of daily mean quantities for 29 February 2020 along the Ikertivaq valley and through the ST (Figure 4) illustrate the air-sea interactions in the ST in more detail.

On 29 February 2020, the superimposed strong pressure gradients associated with the polar low cause velocities that reach almost 50 m s^{-1} over the steep slopes near the coast and result in a tongue of high wind speeds reaching up to 30 m s^{-1} in the lower 1,000 m over the shelf (Figure 4a). Where the slopes are steepest, there is a hydraulic

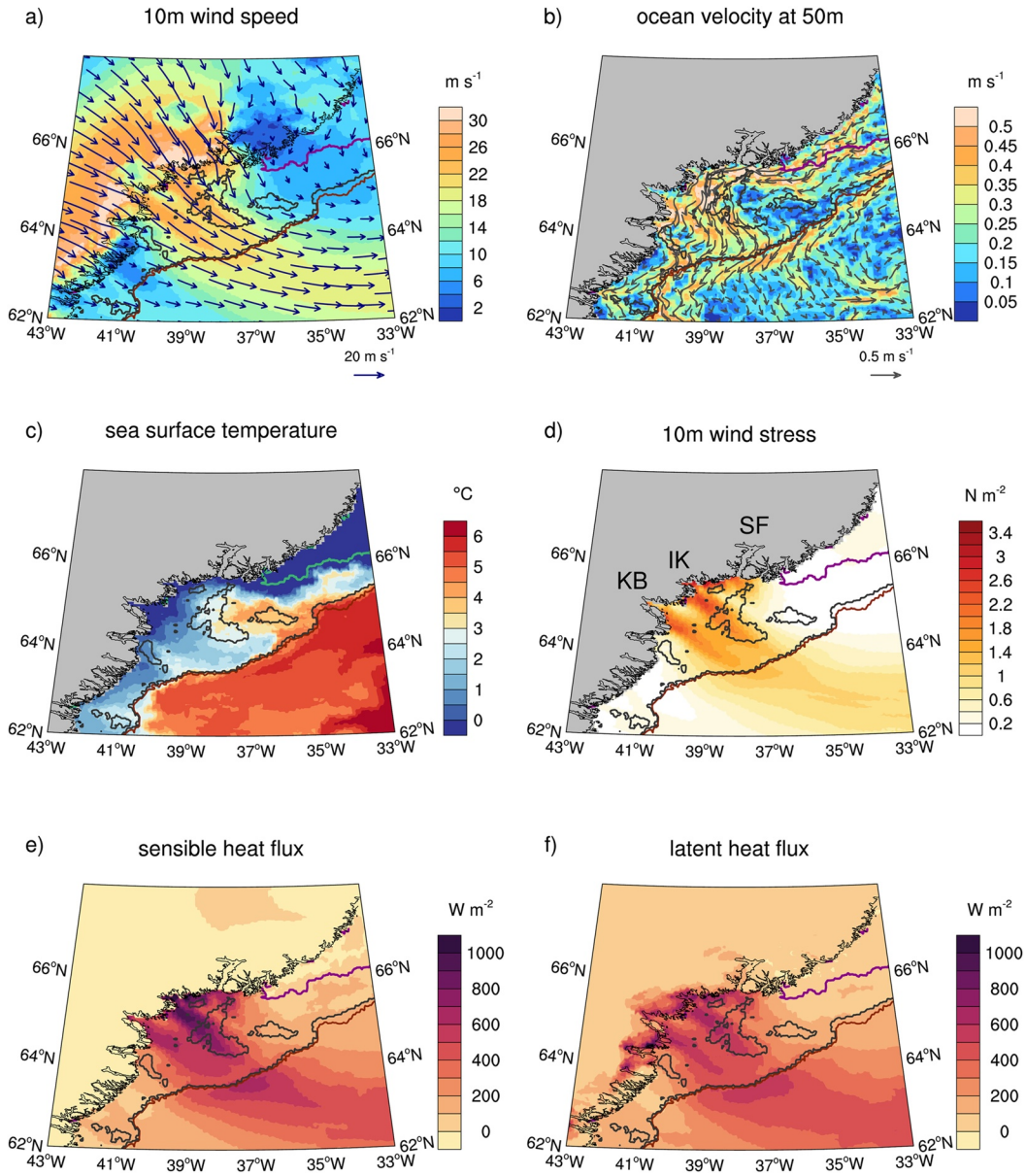

Figure 3. Air-sea interactions (daily means) in the Ammassalik area: (a) 10 m wind speed (shaded color) and vectors, (b) ocean velocity at 50 m depth (shaded color) and vectors, (c) sea surface temperature, (d) 10 m wind stress, (e) sensible heat flux, and (f) latent heat flux. Overlain are the 500 and 1,000 m isobaths (brown and gray contours) and the 15% sea ice concentration [green in (a and c), magenta in all other]. The fjord names in Ammassalik are indicated in (d) with KB: Køge Bugt Fjord, IK: Ikertivaq, and SF: Sermilik Fjord.

jump and the wind speed drops to very small values. This jump is associated with the breaking of a mountain wave as described in Oltmanns et al. (2015). The breaking mountain wave transfers momentum downwards, which can be seen by strong downward velocities (Figure 4c) that accelerate the katabatic flow (see details how this affects the dynamics of the katabatic flow in Oltmanns et al. (2015)).

Over the ocean, the cold and dry air mass from the Greenland ice sheet (Figure 4e) encounters the relatively warm water of the ST (Figure 4d). Convection with cloud formation is initiated in the atmosphere due to unstable stratification (Figure 4c). The clouds, however, move quickly with the flow or dissolve because of the descending dry air, so only a small fraction is visible in the daily mean. The katabatic boundary layer is well visible from the potential temperature distribution (Figure 4e) and is about 200–400 m thick, which is typical for southeast

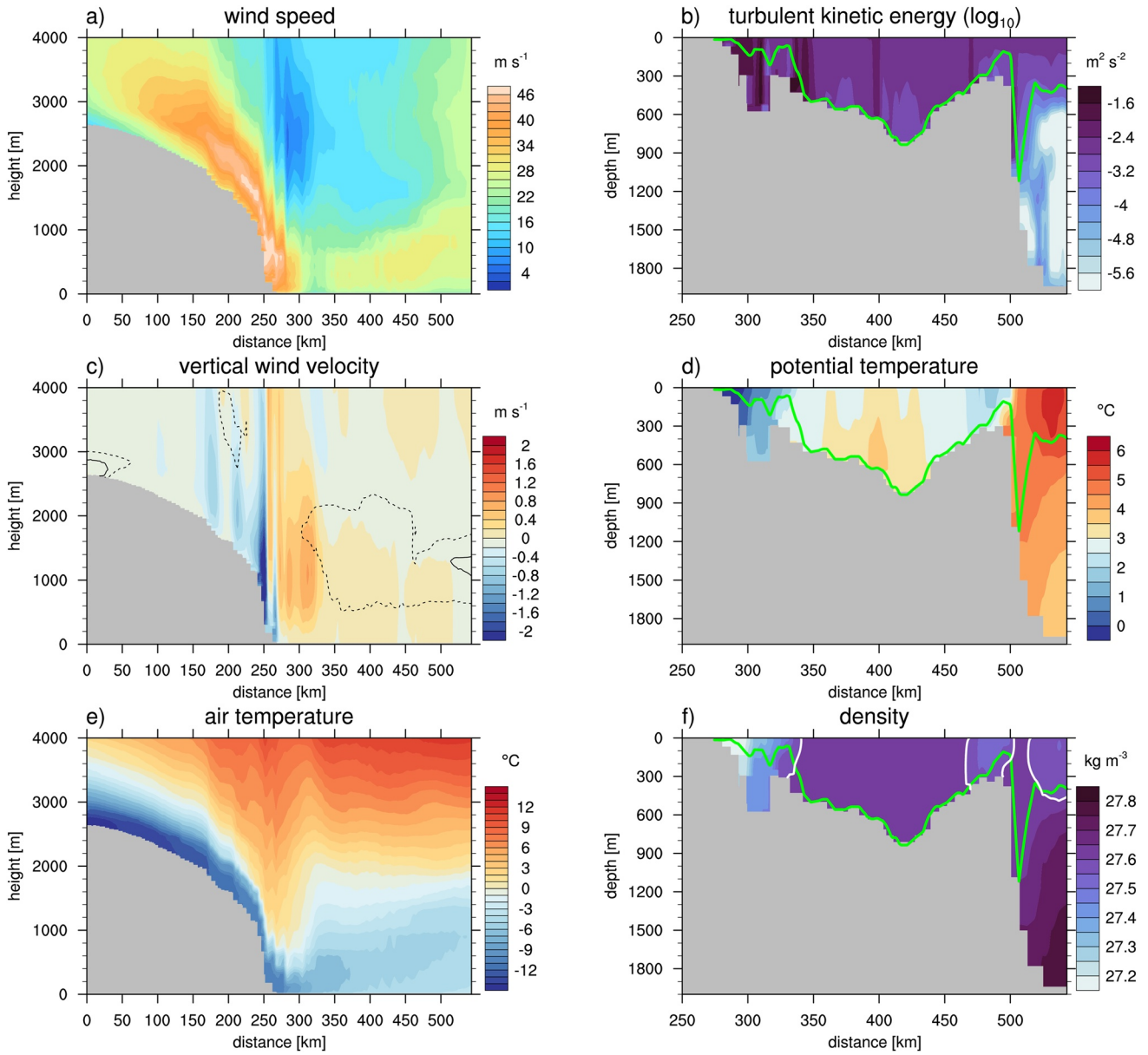

Figure 4. Vertical transects (daily means) along the Ikertivaq valley and Sermilik Trough: (a) wind speed, (b) turbulent kinetic energy in ocean, (c) atmospheric vertical velocity with cloud cover (10% dashed and 50% solid contours), (d) ocean potential temperature, (e) atmospheric potential temperature, and (f) ocean density ($\sigma_\Theta = \sigma - 1{,}000$ kg m^{-3}, $\sigma_\Theta = 27.6$ kg m^{-3} as white contour). The green line in (b, d, and f) marks the depth of the mixed layer ($\sigma_\Theta = 0.03$ kg m^{-3}).

Greenland (Heinemann, 2003; Klein & Heinemann, 2002). As the cold and dry air mass warms and moistens over the shelf, the stable boundary layer evolves into a convective boundary layer, whose height increases with distance from the coast. The cold air outburst and the subsequent convection and cloud formation could also further intensify the polar low because of latent heat release.

Strong wind stress and heat fluxes cause intense vertical mixing and buoyancy loss in the ST (discussed in detail in Section 4), resulting in large values of TKE (Figure 4b) reaching 10^{-2} m^2 s^{-1} near the surface. In fact, the entire water column in the ST is mixed, as can be seen from the mixed layer reaching the bottom and the homogeneous density (Figure 4f) with the 27.6 kg m^{-3} isopycnal outcropping at the surface. However, the water mass is not homogeneous as there is still structure in the temperature and salinity fields. The heat loss and the subsequent cooling results in mixed layer densities of about $\sigma_\theta = 27.6$–27.65 kg m^{-3}. The density of the formed water on the

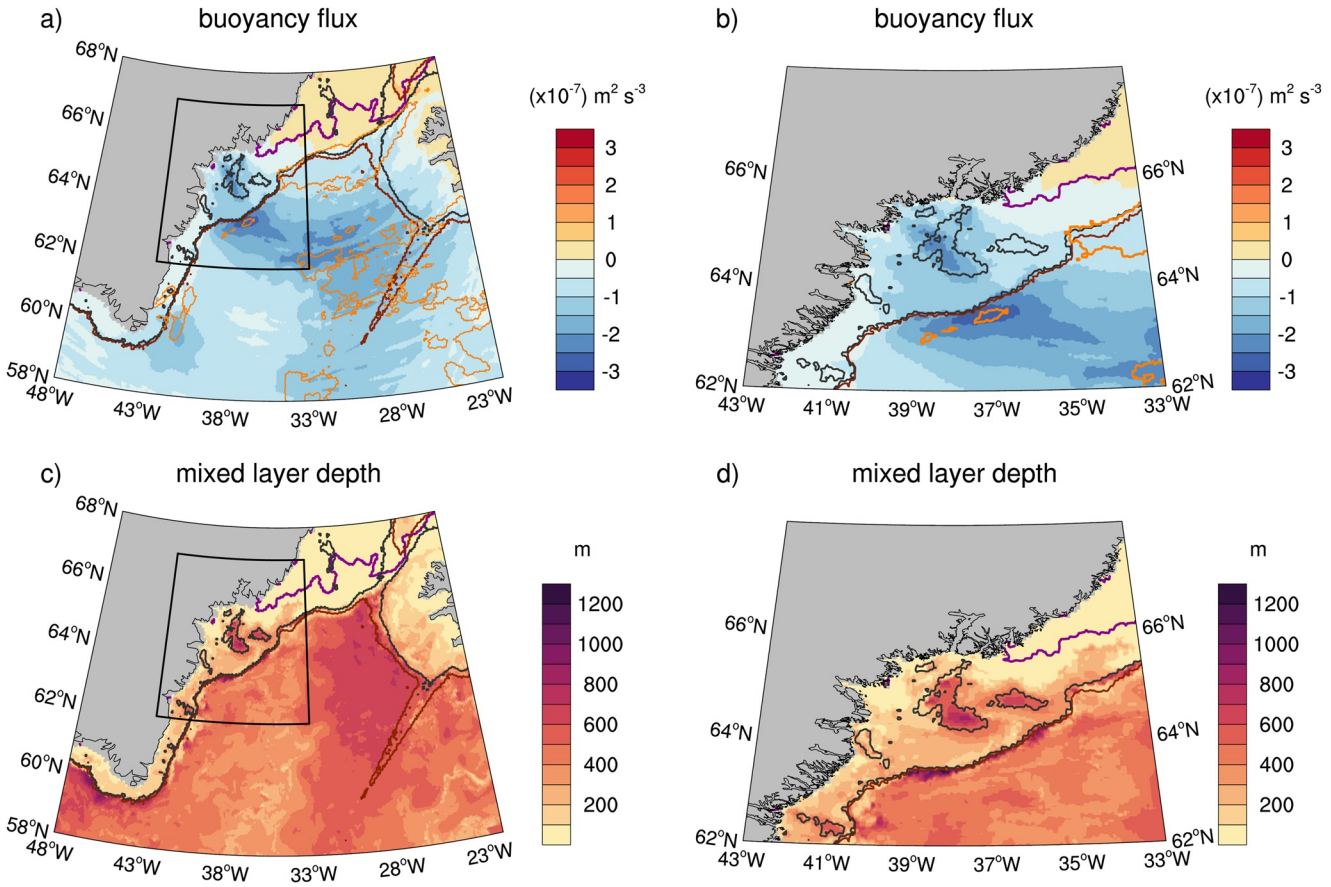

Figure 5. Mixed layer depth ($\sigma_\theta = 0.03$ kg m^{-3}) in (a) the Irminger Sea and (b) Ammassalik area (defined as the black box), and buoyancy flux in (c) the Irminger Sea and (d) Ammassalik area during the katabatic storm on 29 February 2020. The orange contours in (c) and (d) enclose areas where the standard deviation of the buoyancy flux $\hat{\sigma}(B) \geq 0.5 \cdot 10^{-7}$m^2 s^{-3}. Overlain are the 500 and 1,000 m isobaths (brown and gray contours) and the 15% sea ice concentration (magenta contours).

shelf and shelf break is close to the recently identified uISIW ($\sigma_\theta = 27.65$–27.73 kg m^{-3}; LeBras et al., 2020) and is dense enough to contribute to the lighter upper NADW (Li et al., 2021).

The relatively warm temperatures of the EGIC induce a secondary peak of turbulent heat flux and negative buoyancy flux at the shelf break, leading to densities in the boundary current similar to those in the ST and a mixed layer depth of about 1,100 m. The mixed layer depth is defined as the depth where the potential density deviates by $\sigma_\theta = 0.03$ kg m^3 from the surface density. Dense water then leaves the ST and flows into the lower boundary current over the course of the next couple of days (not shown). Both processes cause a densification of the boundary current and thus contribute to the sinking of Atlantic water in the Irminger Sea. The density anomalies are then transported downstream where they can even reach the Labrador Sea.

4.3. Buoyancy Flux and Mixed Layer Depth

The considerable heat loss from the ocean and momentum gain due to high wind stress leads to convection and vertical mixing in the ST and on the shelf break, which is visible as deep mixed layers ($\sigma_\theta = 0.03$ kg m^3; Figures 5a and 5b) in the ST and as a narrow band along the shelf break. On a larger scale, there are mixed layer depths of about 700 m along the western flank of the Reykjanes Ridge (Figure 5a). In the southwest Irminger Sea, the depths of the mixed layer are about 400–600 m, confined to the area of the Irminger Gyre. In the central basin, mesoscale activity and eddies prevent deeper mixed layers. This pattern of mixed layer depths reflects well the mean condition in winter 2020 (not shown), without exceptional deep convection in the southwestern Irminger Sea.

To quantify the effect of the katabatic storm on the ocean, we calculated the buoyancy flux (B) following Groeskamp et al. (2019), with a negative B meaning buoyancy loss of the ocean:

$$B = \overline{w'b'} = \frac{g\alpha}{\rho_0 c_p} Q_0 + g\beta S(P - E), \tag{2}$$

with g the gravitational acceleration, $\rho_0 = 1025.022$ kg m^{-3} the reference density, Q_0 the net heat flux (in W m^{-2}) at the ocean surface (positive into the ocean), α and β the thermal expansion and haline contraction coefficients, S the salinity, P the precipitation (in m s^{-1}), and E the evaporation (in m s^{-1}). Note that we neglect the penetration of shortwave radiation into the ocean, as it is anyway very small in winter. The net heat flux at the ocean surface was calculated as:

$$Q_0 = Q_S + Q_L + Q_{SW} + Q_{LW}, \tag{3}$$

with Q_S the sensible heat flux, Q_L the latent heat flux, Q_{SW} the net shortwave radiation, and Q_{LW} the net longwave radiation.

The buoyancy loss is mainly determined by the turbulent heat fluxes. It peaks over the ST and EGIC where the turbulent heat fluxes are largest, but there is also buoyancy loss in the central Irminger Basin (Figures 5a and 5b).

Although there is no exceptional open-ocean deep convection (>1,000 m) in the southwestern Irminger Sea during the simulated winter, these results suggest that katabatic storms can contribute to precondition the Irminger Sea for convection. In contrast, a tip jet at Cape Farewell occurring at the same day induces buoyancy loss only near the coast. From the standard deviation of the buoyancy flux in winter 2020, there are clear imprints of the mesoscale wind systems. East of Cape Farewell from tip jets, from katabatic storms off the shelf break in the Ammassalik area, and a larger area south of the sea ice edge in relation to marine cold air outbreaks induced by barrier winds.

4.4. Water Mass Transformation and Role of the Katabatic Storm on 29 February 2020

We estimate the water mass transformation $F(\sigma; \mathrm{m}^3\ \mathrm{s}^{-1})$ for density classes (or bin sizes) enclosed by outcropping isopycnals of $\Delta\sigma = 0.05$ kg m^{-3}, following the approach of Petit et al. (2020) and Speer and Tziperman (1992). We calculate $F(\sigma)$ from daily mean values of the buoyancy flux:

$$F(\sigma) = \frac{1}{(g/\rho_0)\,\Delta\sigma} \iint -B\,\Pi(\sigma)\,dA, \tag{4}$$

where

$$\Pi(\sigma) = \begin{cases} 1, & \text{for } |\sigma - \sigma'| \le \dfrac{\Delta\sigma}{2} \\ 0, & \text{otherwise} \end{cases} \tag{5}$$

ensures that only the area A enclosed by a density class is integrated. $F(\sigma) > 0$ means that water is transformed to this density class. We chose $\Delta\sigma = 0.05$ kg m^{-3} and show the result for the densest outcropping class of $\sigma = 27.6 \pm \Delta\sigma/2$ kg m^{-3}.

Figure 6a shows the integrated water mass transformation (WMT) for density class $\sigma = 27.6 \pm 0.025$ kg m^{-3} in winter 2020 (January 20 to April 30). The WMT is largest along the narrow boundary current, which follows the shelf break from Denmark Strait around Cape Farewell. In the southwestern Irminger Sea, the area of WMT widens to the east and includes the Irminger Gyre. Eastern extensions of elevated WMT are likely associated with westerly tip jets, which densify the center of the Irminger Gyre and can trigger open-ocean convection (Våge et al., 2011). A similar peak is seen west of Cape Farewell, probably associated with easterly or reverse tip jets (Moore & Renfrew, 2005). The Irminger shelf makes a significant contribution to the WMT, including the Sermilik Trough. Finally, there is also WMT southwest of Iceland, where a branch of the IC, or from a direct crossing of the East Reykjanes Ridge Current (e.g., Daniault et al., 2016), flows from the Reykjanes Ridge through Denmark Strait into the Nordic Seas, becoming the North Iceland Irminger Current.

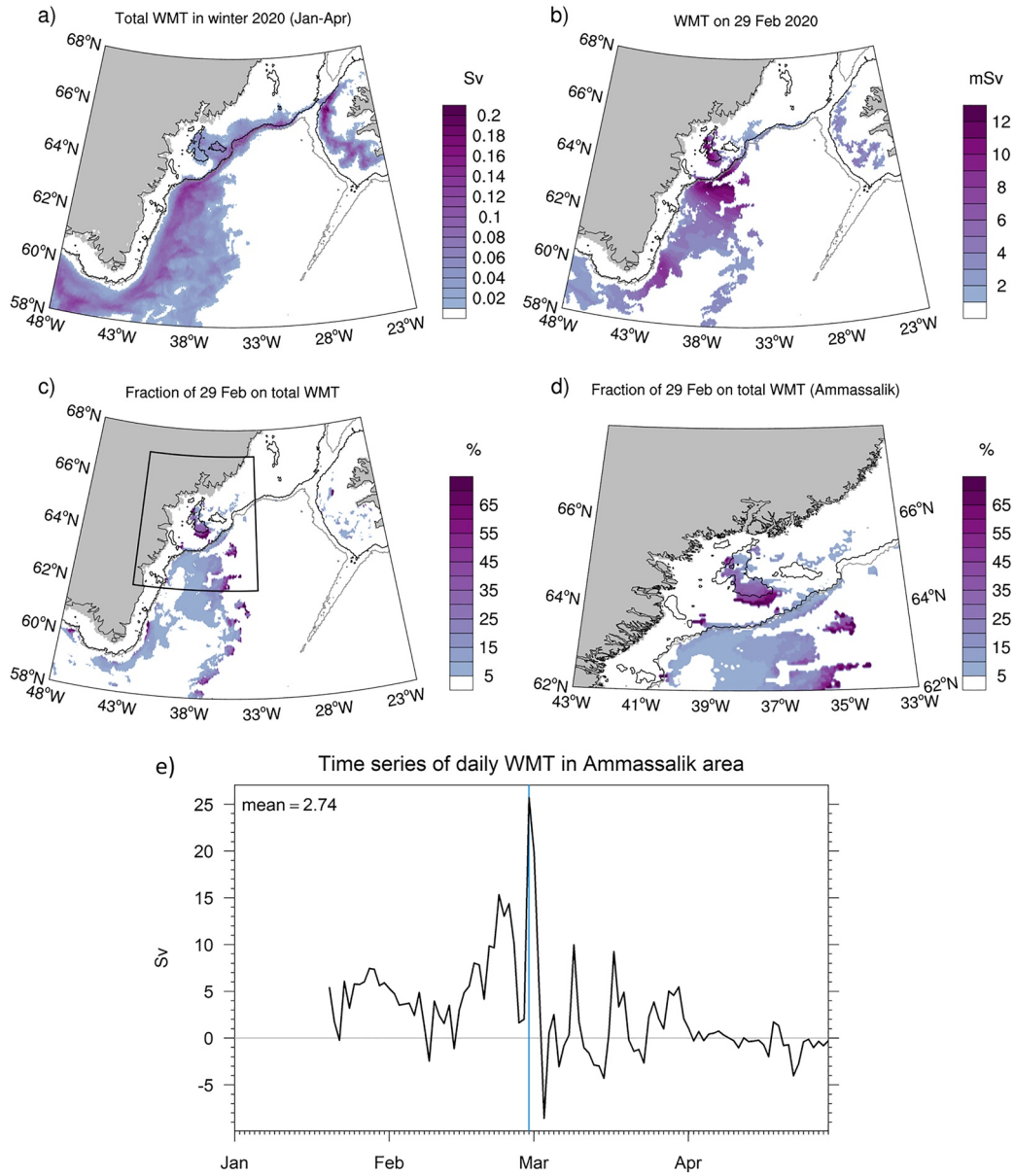

Figure 6. Water mass transformation (WMT) of density class $\sigma = 27.6 \pm 0.025$ kg m^{-3} (a) accumulated over winter 2020 (20 January to 30 April) and (b) on 29 February 2020 during the katabatic storm. The fraction of the WMT on 29 February on the total WMT in winter 2020 (20 January to 30 April) is shown in (c) for the Irminger Sea and (d) for the Ammassalik area defined as the black box in (c). The colored contours show the 500 m (black) and 1,000 m (gray) isobaths. (e) time series of water mass transformation of same density class integrated over the Ammassalik area (black box in c). The 29 February 2020 is marked by the vertical blue line.

On 29 February 2020, there are two areas with strong WMT (Figure 6b). Water mass transformation is largest in the ST and along the EGIC induced by the katabatic storm, with an area downstream that also includes part of the inner basin. The second but weaker peak is induced by the tip jet southeast of Cape Farewell. To estimate the significance of the katabatic storm, we calculated the proportion of the WMT on February 29 to the total WMT in winter 2020 (Figure 6c). We find that the WMT during the katabatic storm accounts for about 10–20% of the total WMT along the shelf break in the Ammassalik area (Figure 6d) and up to 70% in the ST. Integrating over the area shown as a black box in Figure 6c and considering the period from 20 January to 30 April 2020 shows that water mass transformation peaks during the katabatic storm. A day later, on 1 March, the Ammassalik area is still influenced by the storm and water transformation remains high before dropping sharply after the storm subsides.

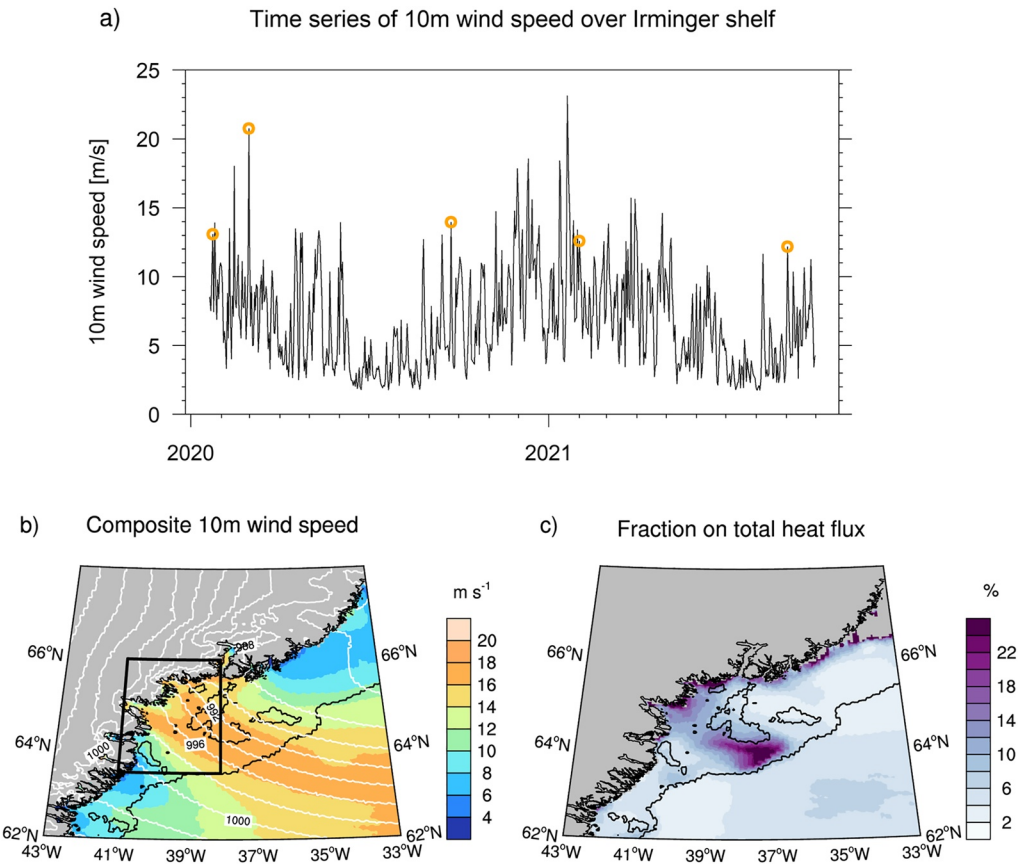

Figure 7. Cases of katabatic storms in ICON-ESM (5 km). (a) Time series of daily mean of 10 m wind speed averaged over the black boxes shown in (b), the orange dots mark the identified katabatic storms; (b) composite of daily mean 10 m wind speed (color shaded) and mean-sea level pressure (white contours) from all five cases in 2020 to 2021; and (c) fraction of net heat flux during katabatic storms on the total heat flux. The 500 m isobath is shown as gray contours in (b) and (c).

The net WMT for density class $\sigma = 27.6 \pm \Delta\sigma/2$ kg m^{-3} is about 2.74 Sv in winter 2020. The water mass formed can be considered as contributing to the lower limb of the AMOC as its density lies below the isopycnal of maximum overturning for OSNAP-East ($\sigma_\theta = 27.55$ kg m^{-3}, Li et al., 2021; Lozier et al., 2019), which is also referred to as the lightest uNADW. Even though we have analyzed only a single event so far, the role of katabatic storms for triggering deep convection are underestimated simply because the atmospheric resolution has so far been too coarse to resolve them. These results suggest that katabatic winds could be of greater importance than has been attributed to them so far, for example, by Paquin et al. (2016).

5. Role of Katabatic Storms for Heat Loss Over the Irminger Shelf

In the previous section, we have focused on a particular katabatic storm. In the following, we expand the picture and analyze how important such katabatic storm events are for heat loss over the Irminger shelf. Our simulation may not be representative of the variability and frequency of occurrence of katabatic storms, but we will relate all occurring katabatic storms in the model to the entire simulation period.

We apply a detection algorithm to identify katabatic storms like the one on 29 February 2020. A katabatic storm is identified when the daily mean 10 m wind speed averaged over the black box shown in Figure 7 exceeds the threshold of 12 m s^{-1} (grid boxes over land were omitted). The threshold was chosen as the spatially averaged 90th percentile of 10 m wind speed considering the entire simulation length. Further, we defined a wind corridor and only count days when wind direction is from northwest between 270° and 360°. We exclude winds from north-north east out of Sermilik Fjord to avoid mixture with barrier winds that have the same northeasterly wind direction. Finally, we count events only when they are 24 hr separated. However, we note that it might also be

justified to ignore this criterion, since events lasting longer than 1 day are also relevant for heat loss (e.g., in our case study). We further note that there is 6-hourly data available for wind speed and direction from 20 January to 29 February 2020 according to the DYAMOND protocol (Stevens et al., 2019), but only daily values thereafter to save disk space.

Using this threshold, we identify five katabatic storm events during the entire simulation (Figure 7a). Three events in 2020 on 23 January 29 February and 29 September and two events in 2021 on 1 February and 2 September. These are fewer events than reported by for example, Oltmanns et al. (2014), who found about 8 events per year based on a station in the Sermilik Fjord and about seven events from ERA-Interim. The reason for this difference is likely that we use spatial averages of daily wind speed, while Oltmanns et al. (2014) used subdaily wind speeds at the station location, resulting in more frequent high wind speeds. The detection of katabatic storms or strong downslope events is hence sensitive to the chosen threshold and domain. The wind corridor choice, however, is rather stable, because the winds have to follow the geographical orientation of the valleys. The composite 10 m wind speed of all events is shown in Figure 7b. The pattern resembles those of the case study with composite wind speeds of about 16–20 m s^{-1} in the cores, reaching into the interior basin of the Irminger Sea.

We find that katabatic storms occur on about 0.8% of the simulation days (2% of the days in winter 2020 (20 January to 30 April)). Calculating the ratio between the net heat loss (3) during katabatic storms and the total heat loss integrated over the entire simulation length shows that they account for up to 25% of the total heat loss over the shelf and about 5% over the open Irminger Sea (Figure 7c). Counting only the two cases in winter 2020, we find that they account for about 15% of the winter heat loss over the shelf (not shown). These numbers are consistent with the results of Oltmanns et al. (2014), according to which about one fifth of the total heat loss in winter is due to katabatic storms.

6. Summary and Conclusions

We have analyzed a strong mesoscale katabatic storm event over the Irminger Sea and how it interacts with the ocean in the fully coupled, global climate model ICON-ESM with storm-resolving and eddy-resolving (5 km) resolution. Katabatic storms have not been resolved in global models because of their small spatial extent, especially in the narrow valleys and fjords of Greenland. Our study is the first to simulate such an event and its interactions with the ocean and feedbacks with large-scale synoptics in a global coupled climate model.

ICON-ESM is able to represent katabatic storms and other mesoscale wind systems around Greenland with details previously described only by regional climate models. It captures the complex interaction of the circulation with the steep orography of southeast Greenland. A polar low forms within a lee trough environment over the Irminger Sea that is initially triggered by the katabatic flow from the Ammassalik valleys. The superimposed pressure gradient of the polar low accelerates the katabatic flow into a storm but also deepens the upper-level trough. These results demonstrate the importance of resolving the feedback of the small scales to the large scale in global climate models and emphasizes the synoptic relevance of the Irminger Sea.

High resolution in the ocean allows resolving small-scale bathymetric features of the southeast Greenland shelf, such as the ST, where the EGC interacts with the EGCC and where water mass transformation takes place. Strong air-sea fluxes caused by the katabatic storm induce substantial heat loss from the ocean and transfer momentum to it. As a result, convection and mixing is induced in the ST and along the shelf break, leading to density anomalies in the trough and boundary current. Previous studies have shown that density anomalies in the boundary current of the Irminger Sea caused by surface fluxes strongly influence AMOC variability. This picture agrees with recent observations, which suggest that it is rather convection and density anomalies in the western boundary current than convection in the basin interior that affects AMOC variability (Li et al., 2021).

The water mass formed within the ST and on the shelf during the katabatic storm has a density of about $\sigma_\theta = 27.6$ kg m^{-3} that is close to the recently described upper Irminger Sea Intermediate Water (LeBras et al., 2020) and can be considered as contributing to the lower limb of the AMOC as its density lies below the isopycnal of maximum overturning for OSNAP-East ($\sigma_\theta = 27.55$ kg m^{-3}, Li et al., 2021; Lozier et al., 2019), which is also referred to as the lightest upper North Atlantic Deep Water. We identify five katabatic storms occurring on 0.8% of the simulation days that account for up to 25% of the heat loss over the Sermilik Trough. Limited to winter 2020 (January-April), the two detected katabatic storms account for about 20% of the total heat loss. The storm

on 29 February 2020 thereby caused roughly 70% of the dense water formation in the ST and about 10–20% at the shelf break and on its seaward side.

Even though our simulation is rather short, we find that katabatic storms are relevant for the densification of the western boundary current. Experiments covering several decades with this class of models will be carried out in the European Union "NextGEMs" project (https://nextgems-h2020.eu). These simulations provide opportunities to explore further how dense water masses formed in the ST and at the shelf break together with denser water masses from deep convection and overflows contribute to North Atlantic Deep Water and its variability.

We conclude that katabatic storms contribute substantially to the formation of dense water in the western boundary current of the Irminger Sea. Resolving them in global climate models is therefore important for the variability of the lower limb of the AMOC, but also for feedbacks with the synoptic-scale atmospheric circulation, especially with respect to the formation of polar lows.

Data Availability Statement

Open Research Primary scripts to reproduce the figures and analyses can be obtained from MPG.PuRe (http://hdl.handle.net/21.11116/0000-0008-ECF1-E, Gutjahr et al. (2021a) and the model data from the WDCC Long Term Archive (http://cera-www.dkrz.de/WDCC/ui/Compact.jsp?acronym=DKRZ_LTA_033_ds00010, Gutjahr et al., 2021b). The model code of ICON is available to individuals under licenses (https://mpimet.mpg.de/en/science/modeling-with-icon/code-availability). The buoyancy fluxes and the water mass transformation were calculated with R 4.0.2 (R Core Team, 2020) and the oce package version 1.3-0 (Kelley & Richards, 2021).

Acknowledgments
This work is a contribution to the project S2 (Improved Parameterizations and Numerics in Climate Models) of the Collaborative Research Centre TRR 181 "Energy Transfer in Atmosphere and Ocean" funded by the Deutsche Forschungsgemeinschaft (DFG, German Research Foundation)—Project number 274762653 and the Max Planck Society for the Advancement of Science. The research was supported by the European Union Horizon 2020 collaborative project NextGEMS (Grant No. 101003470). DYAMOND data management was provided by the Deutsches Klimarechenzentrum (DKRZ) and supported through the projects ESiWACE and ESiWACE2. The projects ESiWACE and ESiWACE2 have received funding from the European Union's Horizon 2020 research and innovation program under Grant Agreements Nos. 675191 and 823988. This work used resources of the Deutsches Klimarechenzentrum (DKRZ) granted by its Scientific Steering Committee (WLA) under project IDs bk1040 and bb1153. We thank the DYAMOND Winter team at MPI-M and DKRZ (https://www.esiwace.eu/services/dyamond/winter) for producing the simulation. We further thank Elisa Manzini for providing constructive comments and two anonymous reviewers. Open access funding enabled and organized by Projekt DEAL.

References

An, L., Rignot, E., Chauche, N., Holland, D., Holland, D., Jakobsson, M., et al. (2019). Bathymetry of southeast Greenland from oceans melting Greenland (OMG) data. *Geophysical Research Letters*, *46*, 11197–11205. https://doi.org/10.1029/2019GL083953

Bacon, S., Gould, W. J., & Jia, Y. L. (2003). Open-ocean convection in the Irminger Sea. *Geophysical Research Letters*, *30*(5), 1246. https://doi.org/10.1029/2002GL016271

Blanke, B., & Delecluse, P. (1993). Variability of the Tropical Atlantic ocean simulated by a general circulation model with two different mixed-layer physics. *Journal of Physical Oceanography*, *23*(7), 1363–1388. https://doi.org/10.1175/1520-0485(1993)023<1363:VOTTAO>2.0.CO;2

Blechschmidt, A.-M., Bakan, S., & Graßl, H. (2009). Large-scale atmospheric circulation patterns during polar low events over the Nordic seas. *Journal of Geophysical Research*, *114*, D06115. https://doi.org/10.1029/2008JD010865

Bracegirdle, T. J., & Gray, S. L. (2008). An objective climatology of the dynamical forcing of polar lows in the Nordic Seas. *International Journal of Climatology*, *28*, 1903–1919. https://doi.org/10.1002/joc.1686

Bracegirdle, T. J., & Gray, S. L. (2009). The dynamics of a polar low assessed using potential vorticity inversion. *Quarterly Journal of the Royal Meteorological Society*, *135*, 880–893. https://doi.org/10.1002/qj.411

Chafik, L., & Rossby, T. (2019). Volume, heat, and freshwater divergences in the subpolar North Atlantic suggest the Nordic seas as key to the state of the meridional overturning circulation. *Geophysical Research Letters*, *46*, 4799–4808. https://doi.org/10.1029/2019GL082110

Condron, A., Bigg, G. R., & Renfrew, I. A. (2008). Modeling the impact of polar mesocyclones on ocean circulation. *Journal of Geophysical Research*, *113*, C10005. https://doi.org/10.1029/2007JC004599

Daniault, N., Mercier, H., Lherminier, P., Sarafanov, A., Falina, A., Zunino, P., et al. (2016). The northern North Atlantic Ocean mean circulation in the early 21st century. *Progress in Oceanography*, *146*, 142–158. https://doi.org/10.1016/j.pocean.2016.06.007

de Jong, M. F., Oltmanns, M., Karstensen, J., & Steur, L. (2018). Deep convection in the Irminger Sea observed with a dense mooring array. *Oceanography*, *31*, 50–59. https://doi.org/10.5670/oceanog.2018.109

de Jong, M. F., van Aken, H. M., Våge, K., & Pickart, R. S. (2012). Convective mixing in the central Irminger Sea: 2002–2010. *Deep-Sea Research I*, *63*, 36–51. https://doi.org/10.1016/j.dsr.2012.01.003

Desbruyères, D., Mercier, H., Maze, G., & Daniault, N. (2019). Surface predictor of overturning circulation and heat content change in the subpolar North Atlantic. *Ocean Science*, *15*, 809–817. https://doi.org/10.5194/os-15-809-2019

Dierer, S., & Schluenzen, K. H. (2005). Influence parameters for a polar mesocyclone development. *Meteorologische Zeitschrift*, *14*, 781–792. https://doi.org/10.1127/0941-2948/2005/0077

Dipankar, A., Stevens, B., Heinze, R., Moseley, C., Zängl, G., Giorgetta, M., & Brdar, S. (2015). Large eddy simulation using the general circulation model ICON. *Journal of Advances in Modeling Earth Systems*, *7*, 963–986. https://doi.org/10.1002/2015MS000431

Doyle, J. D., & Shapiro, M. A. (1999). Flow response to large-scale topography: The Greenland tip jet. *Tellus*, *51*, 728–748. https://doi.org/10.1034/j.1600-0870.1996.00014.x

DuVivier, A. K., & Cassano, J. J. (2013). Evaluation of WRF model resolution on simulated mesoscale winds and surface fluxes near Greenland. *Monthly Weather Review*, *141*(3), 941–963. https://doi.org/10.1175/MWR-D-12-00091.1

Duyck, E., & de Jong, M. F. (2021). Circulation over the south-east Greenland shelf and potential freshwater export: A drifter study. *Geophysical Research Letters*, *48*, e2020GL091948. https://doi.org/10.1029/2020GL091948

Eady, E. (1949). Long waves and cyclone waves. *Tellus*, *1*, 33–52. https://doi.org/10.1111/j.2153-3490.1949.tb01265.x

Eyring, V., Bony, S., Meehl, G. A., Senior, C. A., Stevens, B., Stouffer, R. J., & Taylor, K. E. (2016). Overview of the coupled model Intercomparison project phase 6 (CMIP6) experimental design and organization. *Geoscientific Model Development*, *9*, 1937–1958. https://doi.org/10.5194/gmd-9-1937-2016

Gaspar, P., Grégoris, Y., & Lefevre, J.-M. (1990). A simple eddy kinetic energy model for simulations of the oceanic vertical mixing: Tests at station Papa and long-term upper ocean study site. *Journal of Geophysical Research*, *95*(C9), 16179–16193. https://doi.org/10.1029/JC095iC09p16179

Giorgetta, M. A., Brokopf, R., Crueger, T., Esch, M., Fiedler, S., Helmert, J., et al. (2018). ICON-A, the atmosphere component of the ICON Earth system model: I. Model description. *Journal of Advances in Modeling Earth Systems*, *10*, 1613–1637. https://doi.org/10.1029/2017MS001242

Giorgi, F. (2019). Thirty years of regional climate modelling: Where are we and where are we going next? *Journal of Geophysical Research: Atmospheres*, *124*, 5696–5723. https://doi.org/10.1029/2018JD030094

Groeskamp, S., Griffies, S. M., Iudicone, D., Marsh, R., Nurser, A. J. G., & Zika, J. D. (2019). The water mass transformation framework for ocean physics and biogeochemistry. *Annual Review of Marine Science*, *11*, 271–305. https://doi.org/10.1146/annurev-marine-010318-095421

Gutjahr, O., & Heinemann, G. (2018). A model-based comparison of extreme winds in the Arctic and around Greenland. *International Journal of Climatology*, *38*, 5272–5292. https://doi.org/10.1002/joc.5729

Gutjahr, O., Jungclaus, J. H., Brüggemann, N., Haak, H., & Marotzke, J. (2021a). Air-sea interactions and water mass transformation during a katabatic storm in the Irminger Sea – Scripts. Retrieved from http://hdl.handle.net/72021.11116/0000-0008-ECF1-E

Gutjahr, O., Jungclaus, J. H., Brüggemann, N., Haak, H., & Marotzke, J. (2021b). Air-sea interactions and water mass transformation during a katabatic storm in the Irminger Sea – ICON Dyamond Winter simulation data. *World data center for climate (WDCC) at DKRZ*. Retrieved from https://cera-www.dkrz.de/WDCC/ui/cerasearch/entry?acronym=DKRZ_LTA_033_ds00010

Haarsma, R. J., Roberts, M. J., Vidale, P. L., Senior, C. A., Bellucci, A., Bao, Q., et al. (2016). High resolution model Intercomparison project (HighResMIP v1.0) for CMIP6. *Geoscientific Model Development*, *9*(11), 4185–4208. https://doi.org/10.5194/gmd-9-4185-2016

Heinemann, G. (2003). Forcing and feedback mechanisms between the katabatic wind and sea ice in the coastal areas of polar ice sheets. *The Global Atmosphere and Ocean System*, *9*(4), 169–201. https://doi.org/10.1080/1023673042000198130

Heinemann, G., & Klein, T. (2002). Modelling and observations of the katabatic flow dynamics over Greenland. *Tellus A: Dynamic Meteorology and Oceanography*, *54*(5), 542–554. https://doi.org/10.3402/tellusa.v54i5.12167

Hersbach, H., Bell, B., Berrisford, P., Hirahara, S., Horányi, A., Muñoz-Sabater, J., et al. (2020). The ERA5 global reanalysis. *Quarterly Journal of the Royal Meteorological Society*, *146*(730), 1999–2049. https://doi.org/10.1002/qj.3803

Hoskins, B. J., McIntyre, M. E., & Robertson, A. W. (1985). On the use and significance of isentropic potential vorticity maps. *Quarterly Journal of the Royal Meteorological Society*, *111*, 877–946. https://doi.org/10.1002/qj.49711147002

Josey, S. A., de Jong, M. F., Oltmanns, M., Moore, G. K., & Weller, R. A. (2019). Extreme variability in Irminger Sea winter heat loss revealed by ocean Observatories initiative mooring and the ERA5 reanalysis. *Geophysical Research Letters*, *46*, 293–302. https://doi.org/10.1029/2018GL080956

Jungclaus, J. H., Lorenz, S. J., Schmidt, H., Brovkin, V., Brüggemann, N., Chegini, F., et al. (2022). The ICON Earth System Model version 1.0. *Journal of Advances in Modeling Earth Systems*, *14*, e2021MS002813. https://doi.org/10.1029/2021MS002813

Kalnay, E., Kanamitsu, M., Kistler, R., Collins, W., Deaven, D., Gandin, L., et al. (1996). The Ncep/ncar 40-year reanalysis project. *Bulletin of the American Meteorological Society*, *77*(3), 437–472. https://doi.org/10.1175/1520-0477(1996)077<0437:TNYRP>2.0.CO;2

Kelley, D., & Richards, C. (2021). oce: Analysis of oceanographic data [Computer software manual]. (R package version 1.3-0). Retrieved from https://CRAN.R-project.org/package=oce

Klaver, R., Haarsma, R., Vidale, P. L., & Hazeleger, W. (2020). Effective resolution in high resolution global atmospheric models for climate studies. *Atmospheric Science Letters*, *21*, e952. https://doi.org/10.1002/asl.952

Klein, T., & Heinemann, G. (2002). Interaction of katabatic winds and mesocyclones near the eastern coast of Greenland. *Meteorological Applications*, *9*, 407–422. https://doi.org/10.1017/S1350482702004036

Kolstad, E. W. (2011). A global climatology of favourable conditions for polar lows. *Quarterly Journal of the Meteorological Society*, *137*, 1749–1761. https://doi.org/10.1002/qj.888

Kolstad, E. W., Bracegirdle, T. J., & Seierstad, I. A. (2009). Marine cold-air outbreaks in the North Atlantic: Temporal distribution and associations with large-scale atmospheric circulation. *Climate Dynamics*, *33*, 187–197. https://doi.org/10.1007/s00382-008-0431-5

Korn, P. (2017). Formulation of an unstructured grid model for global ocean dynamics. *Journal of Comparative Physiology*, *339*, 525–552. https://doi.org/10.1016/j.jcp.2017.03.009

Kristjánsson, J. E., Thorsteinsson, S., Kolstad, E. W., & Blechschmidt, A.-M. (2011). Orographic influence of east Greenland on a polar low over the Denmark Strait. *Quarterly Journal of the Meteorological Society*, *137*, 1773–1789. https://doi.org/10.1002/qj.831

LaCasce, J. H., & Groeskamp, S. (2020). Baroclinic modes over rough bathymetry and the surface deformation radius. *Journal of Physical Oceanography*, *50*, 2835–2847. https://doi.org/10.1175/JPO-D-20-0055.1

Landgren, O. A., Batrak, Y., Haugen, J. E., Støylen, E., & Iversen, T. (2019). Polar low variability and future projections for the Nordic and Barents Seas. *Quarterly Journal of the Royal Meteorological Society*, *145*(724), 3116–3128. https://doi.org/10.1002/qj.3608

LeBras, I. A.-A., Straneo, F., Holte, J., de Jong, M. F., & Holliday, N. P. (2020). Rapid export of waters formed by convection near the Irminger Sea's Western boundary. *Geophysical Research Letters*, *47*, e2019GL085989. https://doi.org/10.1029/2019gl085989

Leduc, M., & Laprise, R. (2009). Regional climate model sensitivity to domain size. *Climate Dynamics*, *32*, 833–854. https://doi.org/10.1007/s00382-008-0400-z

Li, F., Lozier, M. S., Bacon, S., Bower, A. S., Cunningham, S. A., de Jong, M. F., et al. (2021). Subpolar North Atlantic Western boundary density anomalies and the meridional overturning circulation. *Nature Communications*, *12*, 3002. https://doi.org/10.1038/s41467-021-23350-2

Lindzen, R., & Farrell, B. (1980). A simple approximate result for the maximum growth rate of baroclinic instabilities. *Journal of the Atmospheric Sciences*, *37*, 1648–1654. https://doi.org/10.1175/1520-0469(1980)037<1648:ASARFT>2.0.CO;2

Lozier, M. S., Bacon, S., Bower, A. S., Cunningham, S. A., de Jong, M. F., de Steur, L., et al. (2017). Overturning in the subpolar North Atlantic program: A new International ocean observing system. *Bulletin of the American Meteorological Society*, *98*(4), 737–752. https://doi.org/10.1175/BAMS-D-16-0057.1

Lozier, M. S., Li, F., Bacon, S., Bahr, F., Bower, A. S., Cunningham, S. A., et al. (2019). A sea change in our view of overturning in the subpolar North Atlantic. *Science*, *363*(6426), 516–521. https://doi.org/10.1126/science.aau6592

Mc Innes, H., Kristiansen, J., Kristjánsson, J. E., & Schyberg, H. (2011). The role of horizontal resolution for polar low simulations. *Quarterly Journal of the Royal Meteorological Society*, *137*(660), 1674–1687. https://doi.org/10.1002/qj.849

Mc Innes, H., Kristjánsson, J. E., Schyberg, H., & Røsting, B. (2009). An assessment of a Greenland lee cyclone during the Greenland Flow Distortion experiment: An observational approach. *Quarterly Journal of the Meteorological Society*, *135*, 1968–1985. https://doi.org/10.1002/qj.524

Menary, M. B., Jackson, L., & Lozier, M. S. (2020). Reconciling the relationship between the AMOC and Labrador Sea in OSNAP observations and climate models. *Geophysical Research Letters*, *47*, e2020GL089793. https://doi.org/10.1029/2020GL089793

Moore, G. W. K. (2014). Mesoscale structure of Cape Farewell tip jets. *Journal of Climate*, *27*, 8956–8965. https://doi.org/10.1175/JCLI-D-14-00299.1

Moore, G. W. K., & Renfrew, I. A. (2005). Tip jets and barrier winds: A QuikSCAT climatology of high wind speed events around Greenland. *Journal of Climate*, *18*(18), 3713–3725. https://doi.org/10.1175/JCLI3455.1

Moore, G. W. K., Renfrew, I. A., Harden, B. E., & Mernild, S. H. (2015). The impact of resolution on the representation of southeast Greenland barrier winds and katabatic flows. *Geophysical Research Letters*, *42*, 3011–3018. https://doi.org/10.1002/2015GL063550

Moreno-Ibáñez, M., Laprise, R., & Gachon, P. (2021). Recent advances in polar low research: Current knowledge, challenges and future perspectives. *Tellus A: Dynamic Meteorology and Oceanography*, *73*(1), 1–31. https://doi.org/10.1080/16000870.2021.1890412

Neumann, P., Düben, P., Adamidis, P., Bauer, P., Brück, M., Kornblueh, L., et al. (2019). Assessing the scales in numerical weather and climate predictions: Will exascale be the rescue? *Philosophical Transactions of the Royal Society A*, *377*, 20180148. https://doi.org/10.1098/rsta.2018.0148

Oltmanns, M., Straneo, F., Moore, G. W. K., & Mernild, S. H. (2014). Strong downslope wind events in Ammassalik, southeast Greenland. *Journal of Climate*, *27*, 977–993. https://doi.org/10.1175/JCLI-D-13-00067.1

Oltmanns, M., Straneo, F., Seo, H., & Moore, G. W. K. (2015). Role of wave dynamics and small-scale topography for downslope wind events in southeast Greenland. *Journal of the Atmospheric Sciences*, *72*, 2786–2805. https://doi.org/10.1175/JAS-D-14-0257.1

Paquin, J.-P., Lu, Y., Higginson, S., Dupont, F., & Garric, G. (2016). Modelled variability of deep convection in the Irminger Sea during 2003–10. *Journal of Physical Oceanography*, *46*, 179–196. https://doi.org/10.1175/JPO-D-15-0078.1

Petit, T., Lozier, M. S., Josey, S. A., & Cunningham, S. A. (2020). Atlantic deep water formation occurs primarily in the Iceland basin and Irminger Sea by local buoyancy forcing. *Geophysical Research Letters*, *47*, e2020GL091028. https://doi.org/10.1029/2020GL091028

Pickart, R. S., Spall, M. A., Ribergaard, M. H., Moore, G. W. K., & Milliff, R. F. (2003). Deep convection in the Irminger Sea forced by the Greenland tip jet. *Nature*, *424*(6945), 152–156. https://doi.org/10.1038/nature01729

Rasmussen, L. (1989). Greenland winds and satellite imagery (Vol. 32–37). Vejret-Danish Meteorological Society.

R Core Team. (2020). R: A language and environment for statistical computing [Computer software manual]. Retrieved from https://www.R-project.org/dataset

Reinecke, P. A., & Durran, D. (2009). The overamplification of gravity waves in numerical solutions to flow over topography. *Monthly Weather Review*, *137*, 1533–1549. https://doi.org/10.1175/2008MWR2630.1

Rühs, S., Oliver, E. C. J., Biastoch, A., Böning, C. W., Dowd, M., Getzlaff, K., et al. (2021). Changing spatial patterns of deep convection in the subpolar North Atlantic. *Journal of Geophysical Research: Oceans*, *126*, e2021JC017245. https://doi.org/10.1029/2021JC017245

Sampe, T., & Xie, S.-P. (2007). Mapping high sea winds from space: A global climatology. *Bulletin of the American Meteorological Society*, *88*(12), 1965–1978. https://doi.org/10.1175/BAMS-88-12-1965

Simmons, A., & Gibson, J. (2000). *The ERA-40 project plan* (Vol. 3, No. 1, pp. 62). ECMWF. Retrieved from https://www.ecmwf.int/node/12272

Skamarock, W. C. (2004). Evaluating mesoscale NWP models using kinetic energy spectra. *Monthly Weather Review*, *132*(12), 3019–3032. https://doi.org/10.1175/MWR2830.1

Speer, K., & Tziperman, E. (1992). Rates of water mass formation in the North Atlantic ocean. *Journal of Physical Oceanography*, *22*, 93–104. https://doi.org/10.1175/1520-0485(1992)022<0093:ROWMFI>2.0.CO;2

Steele, M., Morley, R., & Ermold, W. (2001). PHC: A global ocean hydrography with a high quality Arctic Ocean. *Journal of Climate*, *14*, 2079–2087.

Stevens, B., Satoh, M., Auger, L., Biercamp, J., Bretherton, C., Chen, X., et al. (2019). Dyamond: The DYnamics of the Atmospheric circulation Modeled on Non-hydrostatic Domains. *Progress in Earth and Planetary Science*, *6*, 61. https://doi.org/10.1186/s40645-019-0304-z

Stoll, P. J., Graversen, R. G., Noer, G., & Hodges, K. (2018). An objective global climatology of polar lows based on reanalysis data. *Quarterly Journal of the Royal Meteorological Society*, *144*(716), 2099–2117. https://doi.org/10.1002/qj.3309

Våge, K., Pickart, R., Sarafanov, A., Knutsen, Ø., Mercier, H., Lherminier, P., et al. (2011). The Irminger Gyre: Circulation, convection, and interannual variability. *Deep-Sea Research I*, *58*, 590–614. https://doi.org/10.1016/j.dsr.2011.03.001

Våge, K., Pickart, R., Thierry, V., Reverdin, G., Lee, C. M., Petrie, B., et al. (2009). Surprising return of deep convection to the subpolar North Atlantic Ocean in winter 2007–2008. *Nature Geoscience*, *2*, 67–72. https://doi.org/10.1038/ngeo382

Van Delden, A., Rasmussen, E. A., Turner, J., & Røsting, B. (2003). Theoretical investigations. In E. A.Rasmussen, & J.Turner (Eds.), *Polar lows: Mesoscale weather systems in the polar regions* (pp. 286–404). Cambridge University Press. https://doi.org/10.1017/CBO9780511524974.005

Yeager, S., Castruccio, F., Chang, P., Danabasoglu, G., Maroon, E., Small, J., et al. (2021). An outsized role for the Labrador Sea in the multidecadal variability of the Atlantic overturning circulation. *Science Advances*, *7*(41), eabh3592. https://doi.org/10.1126/sciadv.abh3592

Xia, L., Zahn, M., Hodges, K. I., Feser, F., & von Storch, H. (2012). A comparison of two identification and tracking methods for polar lows. *Tellus A: Dynamic Meteorology and Oceanography*, *64*(1), 17196. https://doi.org/10.3402/tellusa.v64i0.17196

Zahn, M., & von Storch, H. (2008). A long-term climatology of North Atlantic polar lows. *Geophysical Research Letters*, *35*, L22702. https://doi.org/10.1029/2008GL035769

Zängl, G., Reinert, D., Rípodas, P., & Baldauf, M. (2015). The ICON (ICOsahedral Non-hydrostatic) modelling framework of DWD and MPI-M: Description of the non-hydrostatic dynamical core. *Quarterly Journal of the Royal Meteorological Society*, *141*, 563–579. https://doi.org/10.1002/qj.2378